Pulse compression with planar hollow waveguides: a pathway towards relativistic intensity with table-top lasers

Cord L. Arnold, Bing Zhou, Selcuk Akturk, Shihua Chen, Arnaud Couairon, André Mysyrowicz

Pulse compression with planar hollow waveguides: a pathway towards relativistic intensity with table-top lasers

2010 New J. Phys. 12 073015

(http://iopscience.iop.org/1367-2630/12/7/073015)

New Journal of Physics
The open-access journal for physics

Pulse compression with planar hollow waveguides: a pathway towards relativistic intensity with table-top lasers

C L Arnold[1], B Zhou[1], S Akturk[2], S Chen[1], A Couairon[3] and A Mysyrowicz[1,4]

[1] Laboratoire d'Optique Appliquée, École Nationale Supérieure des Techniques Avancées—École Polytechnique, CNRS UMR 7639, F-91761 Palaiseau Cedex, France

[2] Department of Physics, Istanbul Technical University, Maslak 34469, Istanbul, Turkey

[3] Centre de Physique Théorique, CNRS, École Polytechnique, F-91128 Palaiseau, France

E-mail: Andre.Mysyrowicz@ensta.fr

New Journal of Physics **12** (2010) 073015 (25pp)
Received 5 February 2010
Published 19 July 2010
Online at http://www.njp.org/
doi:10.1088/1367-2630/12/7/073015

Abstract. We study in detail the compression of high-energy ultrashort laser pulses to the few-cycle regime in gas-filled planar hollow waveguides. In this scheme, the laser beam is guided in only one transverse dimension, whereas the other dimension is free to adjust, allowing scalability to high pulse energies. We report on various practical aspects of the planar hollow waveguide compression scheme and characterize the dependence of the performance of the method on several experimental parameters: (i) we evaluate different materials for the construction of planar waveguides; (ii) we investigate the dependence of the pulse duration on gas type and pressure; (iii) we measure the spatial intensity and phase; (iv) we characterize the pulse duration along the transverse beam direction; and (v) we investigate the focusability. An output pulse energy of 10.6 mJ at a duration of 10.1 fs (FWHM) in the beam center after compression is demonstrated. A careful estimation reveals that the radiation should be focusable to a relativistic intensity exceeding 10^{19} W cm^{-2} in the few-cycle regime. The experimental results are supported by numerical modeling of nonlinear pulse propagation inside planar hollow waveguides. We discuss energy up-scalability exceeding the 100 mJ level.

[4] Author to whom any correspondence should be addressed.

Contents

1. Introduction

Compression of ultrashort laser pulses to few- and nearly-single-cycle durations is a crucial effort for certain applications of ultrafast physics and chemistry. Energetic infrared laser pulses of such short durations are important tools for high-field physics [1], acceleration of particles [2], frequency conversion to UV and XUV wavelengths [3], as well as the generation of single attosecond pulses [4]. While the output energy of modern chirped pulse amplification (CPA)-based femtosecond lasers can be as high as several joules, the pulse duration is generally above 20 fs. To obtain shorter pulse duration, external compression schemes are employed based on spectral broadening, mostly via self-phase modulation (SPM). Two methods for spectral broadening and pulse compression are commonly applied: nonlinear propagation inside hollow capillaries filled with a noble gas [5] and self-guided propagation in a noble gas [6]. In both cases, spectral broadening is achieved due to strong SPM, either by external guiding through the capillary or by self-guiding in a filament. Up until now, the maximum output pulse energy for both methods was around 1 mJ. For the hollow capillary scheme the limitation is primarily due to damage of the capillary, especially at high repetition rate, and onset of ionization in the gas. However, by applying a gradient of increasing gas pressure along the capillary, the output energy could be increased [7, 8]. Recently, a compression scheme utilizing the spectral blue shift due to ionization of low-pressure He in a hollow capillary was presented, yielding multi-mJ pulse energy at the expense of the efficiency, which is about 20% [9]. In the filamentation approach, the onset of multiple filamentation and intensity clamping, as well as inherent spatial chirp and angular dispersion of the self-guided pulse, limit the output energy [10]–[12]. It was also shown that only the very core of the filament can be compressed to homogeneous pulse duration [13]. This aspect greatly constrains the output pulse energy for the filamentation compression approach [14].

An alternative approach for high-energy pulse compression is optical parametric chirped pulse amplification (OPCPA) [15, 16]. In this scheme, amplification is achieved by broadband

nonlinear frequency mixing of stretched low-energy seed pulses with high-energy pump pulses. Impressive values of up to 16 TW peak power in the few-cycle regime have been demonstrated recently [17, 18]. However, the OPCPA concept requires elaborate setups and additional high-energy pump lasers.

Nurhuda *et al* [19] recently proposed the compression of ultrashort laser pulses based on SPM inside a gas-filled planar hollow waveguide. In this concept the beam is guided only in one transverse direction. The size of the beam in the perpendicular transverse direction can be freely adapted to adjust the intensity inside the waveguide to a level for efficient SPM, but still below excessive nonlinear ionization. This method offers superior energy scalability as compared to hollow capillaries and filamentation [19]. The technique was experimentally demonstrated first by Chen *et al* [20]. However, in these experiments, it was realized that, in practice, the energy up-scalability of the planar waveguide scheme requires more attention. In particular, small-scale self-focusing causes strong modulations in the spatial beam profile along the free waveguide dimension; the beam thus tends to break up into individual filaments along this dimension. Because of this limitation, the early experiments yielded pulse energies of only ≈ 2 mJ with durations of 12 fs [20]. In more recent work it was shown that, by carefully choosing experimental parameters, such as waveguide length and gas pressure, a trade-off between spatial mode degradation and spectral broadening can be found, allowing significant temporal compression at focusable output beam quality [21]. In these experiments, output pulse energy of 8.1 mJ and duration of 13.6 fs were obtained. Comprehensive simulations of nonlinear propagation in the waveguide, including the interactions in the spatial profile, indicated good agreement with the experiments and suggested the possibility of extending the method to 100 mJ energy levels [22].

In the course of this paper, we present results and a detailed discussion of several practical aspects, as well as the parameter dependence of the pulse compression scheme based on SPM in a planar hollow waveguide. Our discussion includes both experimental and theoretical considerations. In the experimental part, we evaluate various options of assembling planar hollow waveguides, characterize the pulse compression for different types of gases and gas pressures, evaluate the uniformity of pulse compression along the transverse direction, and discuss the spatial intensity and phase of the output beams and their effect on focusability. In the theoretical part we thoroughly present the model employed to simulate nonlinear pulse propagation inside the waveguide. We compare the simulations with the experimental results and discuss possible tuning of experimental parameters for energy up-scalability.

2. Experiments

2.1. Experimental setup

The experimental setup of the planar hollow waveguide pulse compression scheme is illustrated in figure 1. Today's CPA femtosecond lasers can emit pulse energies up to the joule level but pulse durations of typically longer than 20 fs. In our case, the laser (Thales Alpha 100) delivers pulses of energy up to 15 mJ at less than 50 fs duration, 100 Hz repetition rate and about 15 mm beam diameter ($1/e^2$). The planar hollow waveguide is placed inside a gas cell, which can be filled with different noble gases (Ar, Kr and Xe) at adjustable pressure. The input and output windows of the cell are made of thin (1 mm) antireflection-coated fused silica, to minimize dispersion and additional SPM. A cylindrical mirror is used to focus the laser beam to a line at

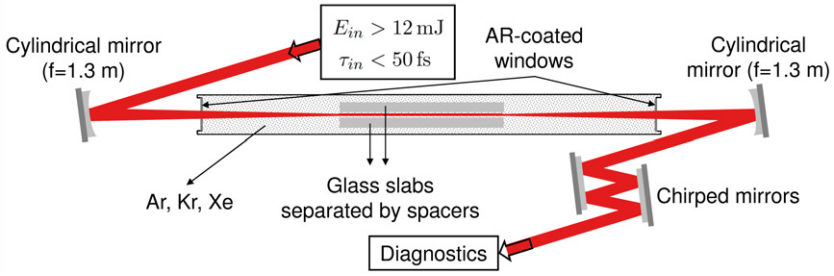

Figure 1. Sketch of the experimental setup for the planar hollow waveguide compression scheme.

the input of the planar hollow waveguide. The cylindrical axis of the focusing mirror needs to exactly coincide with the free transverse axis of the waveguide (where no guiding occurs). To facilitate the alignment, all cylindrical optics are mounted on precision rotation and translation stages. To obtain the best coupling and throughput, the longitudinal waveguide axis must be exactly parallel to the propagation direction of the incoming light and the line focus of the beam should be centered on the short transverse axis of the waveguide. In order to perform the required adjustments, the gas cell is held by xyz-stages at both ends. The polarization of the incoming light is chosen to be along the free waveguide axis, corresponding to transverse electric (TE) guided modes, which feature lower losses than transverse magnetic (TM) modes (see section 3.1). At the output of the cell, the beam is re-collimated by using a second cylindrical mirror, placed one focal distance away from the end of the waveguide. Also, the cylindrical axis of the collimating mirror must be exactly aligned with the focusing cylindrical mirror and the long waveguide axis in order to avoid aberrations. We use broadband dielectric cylindrical mirrors (Eksma, CVI) of focal length $f = 1.3\,\mathrm{m}$, both for coupling the beam to the waveguide and for collimation. After collimation, the beam bounces off a series of chirped mirrors (Femtolasers, Layertec) for spectral phase compensation. Finally, different types of diagnostics are performed. The temporal pulse intensity and phase are measured using a frequency-resolved optical gating (FROG) device, capable of measuring pulses in the single-cycle regime [23]. The spectrum and the pulse energy are monitored with a fiber spectrometer (Ocean Optics HR4000) and an energy-meter (GenTec), respectively. A Shack–Hartmann sensor (Imagine Optics HASO 32) is used to measure wavefront distortions. Finally, a CCD camera (IDS) monitors the laser transverse spatial mode on a white screen placed close to the collimating cylindrical mirror.

2.2. Waveguide construction

The construction of the waveguide constitutes an important practical aspect of the method. In hollow dielectric waveguides, the light is guided due to high reflection coefficients at a grazing angle of incidence. As a result, the supported modes are intrinsically leaky (see section 3.1). However, if the waveguide separation is sufficiently large, the losses can be kept small, allowing high throughput. We assemble our planar hollow waveguides by using two rectangular slabs of glass, separated by thin spacers cut as narrow strips out of a polycarbonate foil (Precision Brand) of homogeneous thickness. We place the spacers along the long edges of the slabs in order to provide as wide a transverse aperture as possible. The inner glass surfaces need to be clean

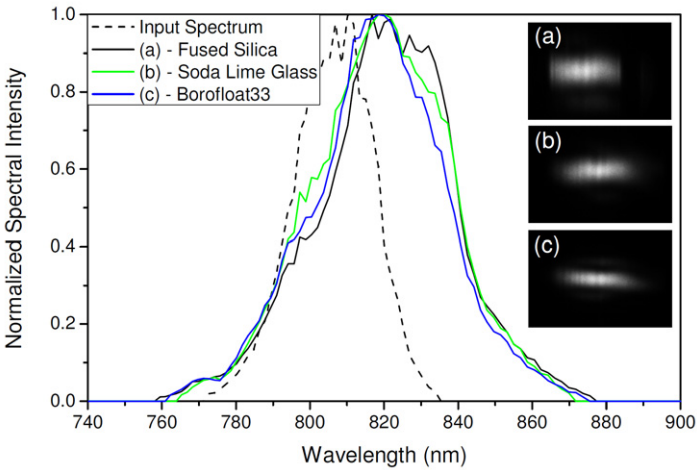

Figure 2. Comparison of spectral broadening and output mode quality for the three different waveguide materials: (a) fused silica, (b) soda lime glass and (c) Borofloat33.

and completely free from dust in order to prevent spatial mode deterioration. The assembly is favorably performed in a clean room environment.

Three different kinds of glass were used to fabricate waveguides. The experimental results published in [21] were obtained with a waveguide made from fused silica of dimensions $19 \times 6 \times 210\,\mathrm{mm}^3$, with all six surfaces polished for each of the two slabs (WZW Optics). The thickness of the spacers used was $127\,\mu\mathrm{m}$. Waveguides of larger dimension still made from fused silica can be quite expensive. We therefore also tested cheaper float glass materials available in a larger size, in particular Borofloat33 (Schott) and soda lime glass (PGO). For the waveguide made from Borofloat33, only the long surfaces constituting the waveguide were polished, the front and side surfaces were cut and the edges were ground. In the case of the soda lime glass, none of the surfaces was treated. The slabs were simply scribe-cut out of a plate of thin (3 mm) soda lime float glass. We first compared the attenuation for the three different kinds of waveguides (with the same slab separation). No significant difference was observed. Since there was no gas cell available to house all three waveguides, the experiments were performed in air. The waveguide made from Borofloat33 has the dimensions $40 \times 10 \times 500\,\mathrm{mm}^3$, whereas the one made from soda lime glass is $40 \times 3 \times 250\,\mathrm{mm}^3$. Next we compared the output spatial modes and spectral broadening for the three waveguides. Since the lengths of the individual waveguides were different, we adjusted the input pulse energy to have comparable spectral broadening. Figure 2 shows the broadened spectra and the associated output spatial modes for the waveguide constructions mentioned above. Spectral broadening is significant in all cases. The distinct red shift of the broadened spectra can be associated with the delayed Kerr response of air [24]. For the waveguide made from soda lime glass, more pulse energy is required in order to obtain comparable broadening. This can be roughly quantified by comparing the values of the B-integral (see section 3.3), which depends on the input pulse energy, the waveguide length and separation, as well as the gas pressure. For soda lime glass, the B-integral value to obtain comparable spectral broadening is about 20% higher as compared to the two other options.

In terms of output spatial mode quality, the waveguide made from all-way polished fused silica glass plates exhibits the best mode quality. A slightly stronger structure is observed for

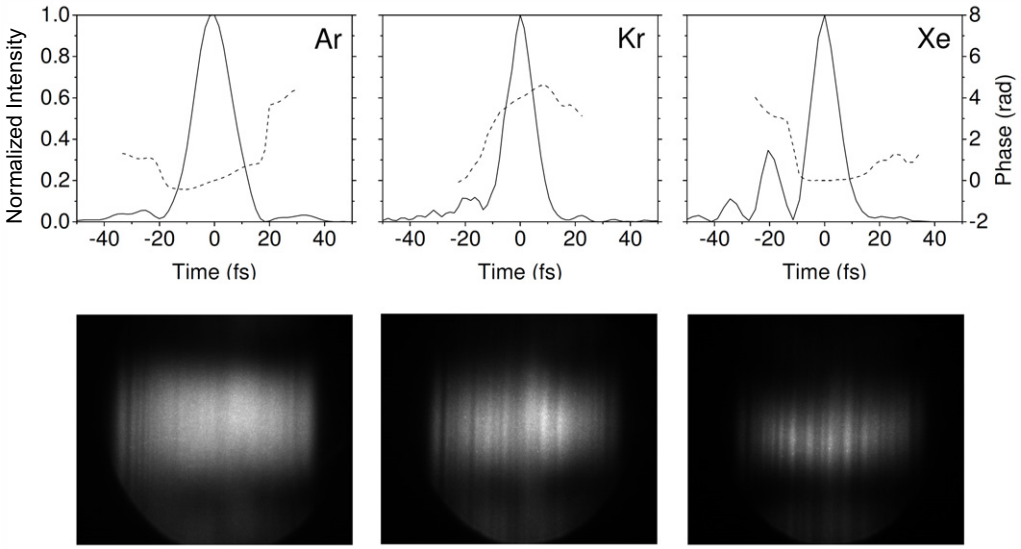

Figure 3. Measured temporal intensity and phase (upper row) and output mode (lower row) for Ar, Kr and Xe (from left to right). Output pulse durations: 16.1, 11.5 and 11.4 fs. Output energies: 8.5, 7.6 and 3.7 mJ.

the two other options (see figure 2). The sharp edges of the spatial output mode profile for the fused silica waveguide are due to beam clipping from the spacers, since the 19 mm width of the waveguide minus the width required for the spacers (about 1 mm on each side) was slightly too narrow for the beam.

For the waveguide made from soda lime glass, we observe dark staining of the glass material at the entrance of the waveguide, after coupling high-power femtosecond pulses into the waveguide. This modification is known to be color center formation due to multiphoton absorption in this type of glass [25]. For Borofloat33 and fused silica, no alterations of the material were observed.

In summary, the best spatial mode quality is obtained with all-way polished fused silica slabs. The float-glass alternatives are significantly lower in cost and easier to fabricate with large dimensions, while slightly compromising the spatial mode quality. For the rest of the paper, the experiments were performed using all-way polished fused silica waveguides.

2.3. Dependence of pulse compression on gas type and pressure

The planar waveguide pulse compression scheme requires strong SPM in order to obtain sufficient spectral broadening. The strength of SPM in the waveguides can be adjusted by using different gases and pressures. On the other hand, as mentioned above, small-scale self-focusing along the free waveguide dimension causes spatial mode deterioration [20]–[22]. Since SPM and small-scale self-focusing both result from the same physical effect (Kerr nonlinearity) in the gas medium, spectral broadening and transverse mode deterioration are closely connected. We compare the hollow planar waveguide compression scheme for the gas cell filled with Ar, Kr and Xe at 1 atm pressure each. The nonlinear refractive index n_2 is the highest for Xe and the lowest for Ar [26]. Figure 3 shows the measured temporal output pulse intensity and phase after compression as well as the spatial mode profiles for the three noble gases. As indicated in the

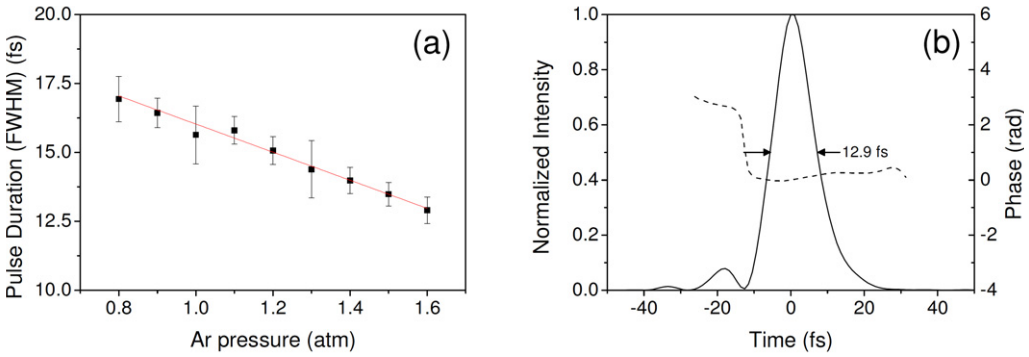

Figure 4. Measured pulse duration after compression versus Ar pressure (a). A typical measured temporal pulse profile after compression at 1.6 atm (b).

figure caption, the duration becomes shorter as the nonlinear index of refraction increases. The shortest pulses were thus obtained in Xe. However, the spatial mode deterioration due to small-scale self-focusing is also the strongest in this case. The input pulse energy for Ar and Kr was ≈ 12.5 mJ (limited by the laser system), while for Xe the input pulse energy had to be reduced to below 6.7 mJ to avoid beam breakup. The output pulse energies were 7.6 and 8.5 mJ for Kr and Ar, respectively, and 3.7 mJ for Xe. As a result, Ar and Kr provide favorable conditions, while Xe exhibits excessive nonlinearity. Furthermore, it should be noted that the ionization potential for Xe (12.13 eV) and Kr (13.99 eV) is lower as compared to Ar (15.76 eV), resulting in higher relative ionization of the gas medium and lower waveguide throughput, which here is 68% for Ar and 61 and 55% for Kr and Xe, respectively. In order to have SPM dominated spectral broadening, plasma formation should be minimized by choosing a gas with high ionization potential. From this simple evaluation we conclude that Ar is the preferable choice of gas for our pulse energy and intensity levels. The possible use of different noble gases will be discussed within the framework of the analysis of stable waveguide propagation and energy scalability presented in section 3.3.

Having identified Ar as the gas of choice, we now study pulse compression as a function of Ar pressure inside the waveguide. Increasing the pressure increases the nonlinear refractive index, and thus both the impact of SPM and small-scale self-focusing. As the deterioration of the spatial output mode compromises the possible compression, a trade-off between the target pulse duration and an acceptable mode quality needs to be found. Here, pressures up to 1.6 atm of Ar were studied, which provide significant shortening at still acceptable output mode quality. Figure 4(a) shows the measured pulse durations after compression as a function of Ar pressure. As expected, the pulse duration becomes shorter with increasing pressure. The energy throughput does not significantly depend on the gas pressure. We observe pulse energies of ≈ 11 mJ at the output of the gas cell, corresponding to a throughput larger than 75% within the whole pressure range. This confirms that the intensity inside the waveguide remains below the level of excessive ionization for Ar. Spectral broadening is thus dominated by SPM and the compressed pulse duration depends linearly on Ar pressure. At a pressure of 1.6 atm, a mean duration of 12.9 fs (full-width at half-maximum (FWHM)) is measured. The temporal profile is very clean, with a prepulse of less than 8% of the peak intensity of the main pulse. Figure 4(b) shows a typical measured temporal intensity profile.

2.4. Variation of pulse duration along the beam transverse dimension

Since SPM and, consequently, spectral broadening are determined by the light intensity in the waveguide, the compressed pulse duration may vary along the non-guided dimension, at least if the transverse beam profile is different from a top-hat. The laser beam profile in our experiments was nearly Gaussian. We hence expect a significant variation in spectral broadening and compressed pulse duration along the free waveguide axis. In order to characterize this effect, a 1 mm wide slit was used, which we moved through the non-guided dimension of the beam in 0.5 mm steps. The broadened output spectrum and the compressed pulse duration were measured as a function of position along the free waveguide dimension. The chirped mirror compression was optimized to obtain the shortest pulse duration in the beam center and kept constant for all other positions. The pressure in the cell containing the waveguide was adjusted to 1.6 atm of Ar and the input pulse energy was slightly above 14 mJ. At the output of the cell, 10.8 mJ was measured before compression and the shortest duration in the beam center was around 10.6 fs (FWHM). Figure 5 shows the output spatial mode (a), the spectrum (b) and the measured pulse duration (c) along the free waveguide dimension. The output spatial mode features significant structure in this experiment, indicating that the Ar pressure is close to the maximum permissible value at this input pulse energy. The spectral broadening clearly follows the transverse beam profile with the broadest spectra generated in the beam center, where the intensity is the highest. The shortest duration is measured close to the beam center as well. Figure 5(d) shows a typical temporal pulse profile measured at the beam center. Due to slightly different experimental conditions and, in particular, a different combination of chirped mirrors for compression, the pulses are shorter here as compared to figure 4, but also exhibit a more pronounced prepulse. Due to limitations in terms of power level and pulse duration for the FROG setup, reliable measurements of the pulse duration were only possible within a 6 mm wide range around the beam center. Although the compressed pulse duration becomes longer towards the edges of the transverse beam profile, the well compressible beam center contains a significant portion of the total beam energy. Within our measurement interval the pulse duration varies from 10.6 fs to about 13 fs (figure 5(c)). This interval of relatively homogeneous pulse duration contains about 67.6% of the total output pulse energy. In terms of possible scalability of the hollow planar waveguide compression scheme to higher pulse energy, it should be mentioned that higher-energy laser systems typically yield beam profiles closer to top-hat, in order to avoid diffraction effects in the gain medium [27]. Considering such a beam profile, the pulse duration would be even more uniform along the beam. The transverse homogeneity in terms of spectrum and duration, as well as the influence of more square-like super-Gaussian beam profiles, will be discussed in detail in the numerical part (section 3.3).

2.5. Spatial phase and focusability

As discussed above, the critical constraint in the planar hollow waveguide compression scheme is the beam characteristics in the free waveguide dimension. To prove that the scheme is indeed useful for applications in high-field physics, we will show that the compressed pulses are focusable to nearly diffraction limited spot size. Here, we discuss the experimentally accessible focusability. A detailed numerical analysis follows in section 3.3. While the guided dimension should focus intrinsically well, the focusability of the free waveguide dimension is compromised. If the light intensity in the free dimension is not uniform, the strength of SPM will vary along the beam, resulting in inhomogeneous spectral broadening and duration

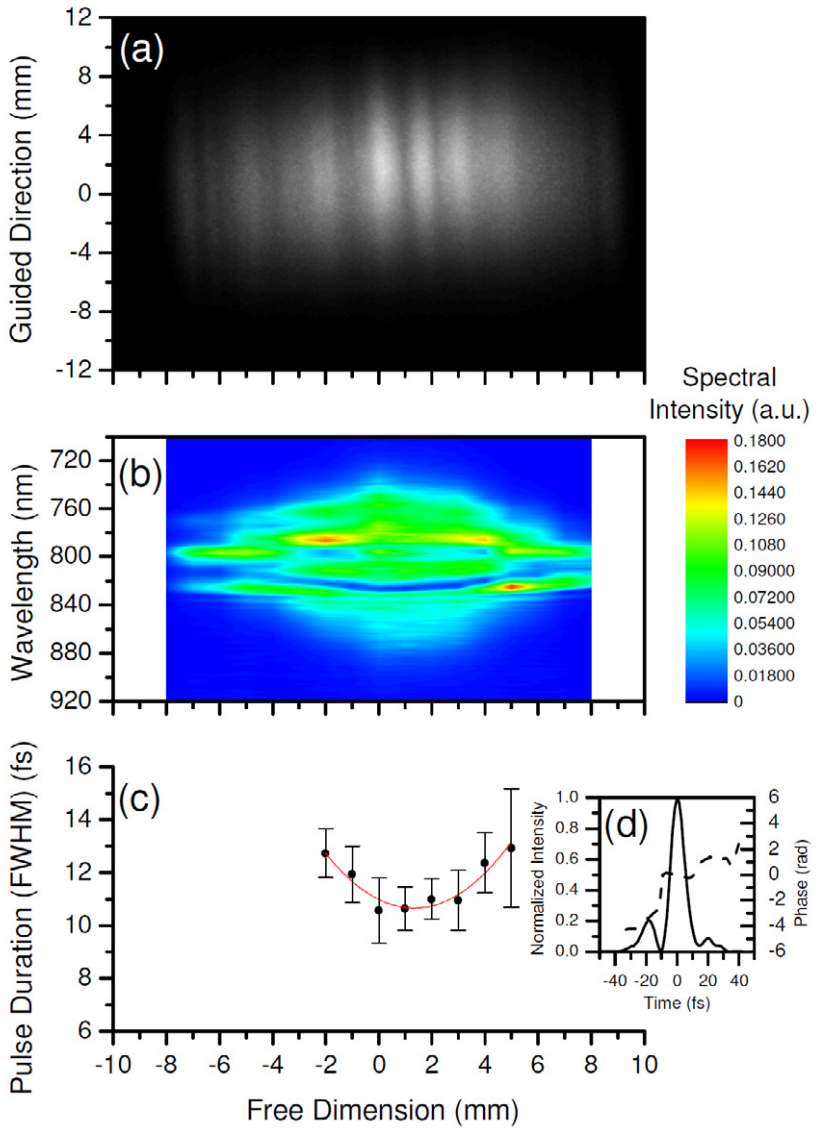

Figure 5. Transverse output profile (a), spectrum (b) and measured pulse duration (c) along the non-guided direction. Typical measured temporal pulse profile in the beam center (d).

after compression. Similarly, because of the intensity-dependent refractive index, high-intensity portions of the transverse profile are retarded, resulting in a spatial phase front and pulse front delay. The transverse phase retardation directly follows the reversed intensity profile in the free waveguide dimension. For a simple Gaussian beam, a parabolic phase delay will be most prominent. This should have two distinct effects. Firstly, the parabolic phase induces an astigmatism, which, if the beam is focused, results in a shift of the focal position towards the laser for the free dimension, whereas the guided dimension focuses further down. Secondly, the beam focuses to a larger (not diffraction limited) spot for the free dimension. In order to study the impact of the spatial phase on the focusability, the spatial phase profile was measured with a Shack–Hartmann wavefront sensor. Since this experiment was performed in air, the input pulse energy was varied instead of the gas pressure, in order to increase or decrease the level of

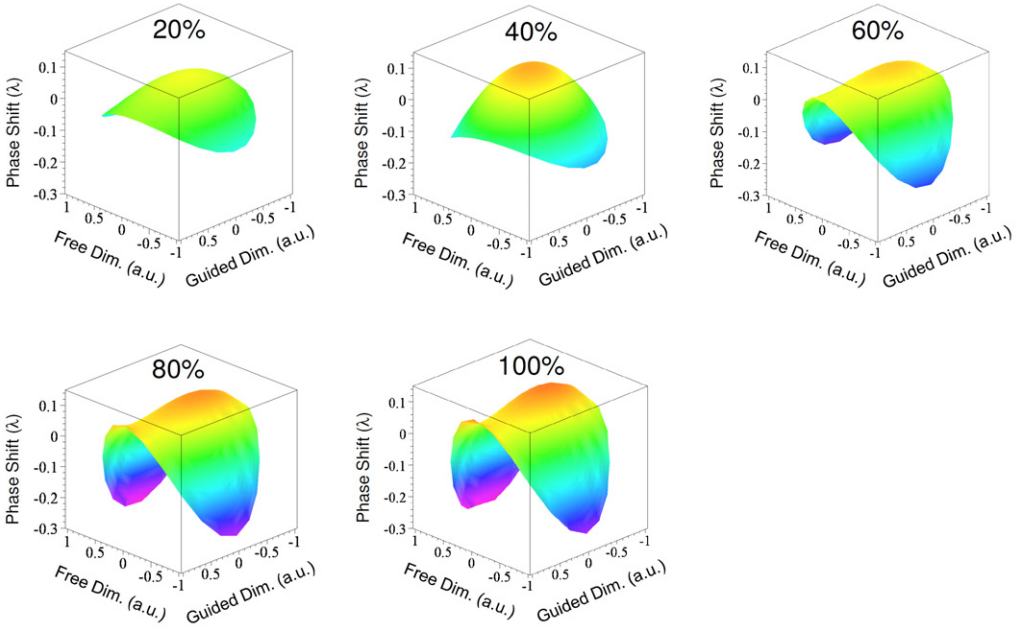

Figure 6. Measured spatial phase profiles (spatial tilt subtracted) at different pulse energy levels.

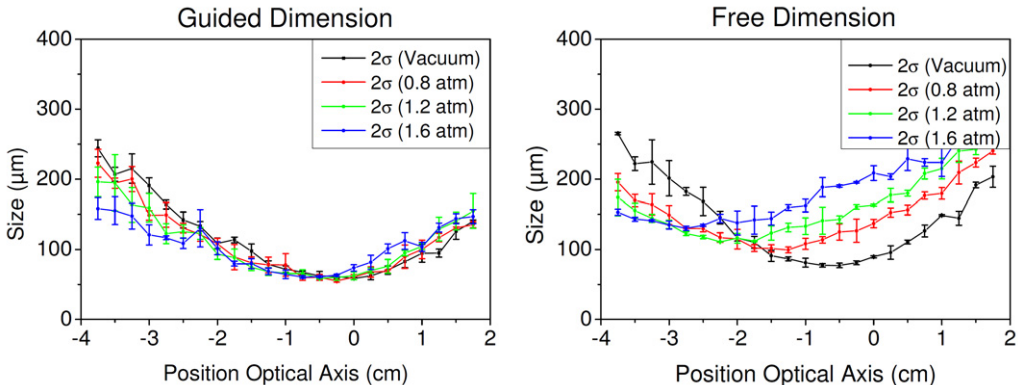

Figure 7. Focal spot radius (second-order moments) versus position on the optical axis for different Ar pressures. Guided waveguide dimension (left). Free dimension (right).

nonlinearity in the waveguide. Figure 6 compares the measured spatial phase profiles (spatial tilt subtracted) for various pulse energies. It is evident that, with increasing pulse energy, the beam develops a strong astigmatism. The high-intensity beam center lags behind and the wave front bends along the free waveguide dimension, whereas the wavefront in the guided dimension remains flat.

In a second measurement the focusability of the output beam was directly investigated. After carefully attenuating the beam by using the reflections from two consecutive fused silica wedges, the beam was focused with a 1 m focal length lens directly onto a CCD camera chip, which could be moved through the focus along the optical axis. Spatio-temporal aberrations due to the thin lens are negligible. Figure 7 compares the focal spot size as a function of

position along the optical axis for the guided and the free waveguide dimensions at various Ar pressures. As expected from the above discussion, the focal spot size of the guided dimension does not change significantly as the gas pressure and thus the nonlinearity in the waveguide is increased. However, for the non-guided dimension we observe a significant shift in the focal position towards the laser as well as a larger focal spot size, as the gas pressure is increased. The focal spot radius $2\sigma(z)$ (plotted in figure 7) was measured by calculating the second-order moments for the guided and the free dimension directly from the CCD images. Moment theory provides a reliable measure of the beam size, even for non-Gaussian transverse profiles. For a Gaussian beam the quantity 2σ is equivalent to the Gaussian beam radius w $(1/e^2)$. For the focal spot sizes presented in figure 7, the quantities 2σ and w were about the same value, indicating that the focal profile was single-peaked and close to Gaussian shape. It must be noted that this method measures the focal spot size of the fluence (intensity integrated over time), whereas the focal intensity profile could, in principle, be different. By performing a parabolic fit for $\sigma^2(z)$, we can estimate the focusability in terms of M^2-values. For the guided dimension, values between 1.3 and 1.5 are found for all pressures, which is reasonable. However, the non-guided dimension exhibits a higher value of $M^2 = 2.33$ already at vacuum. For higher Ar pressures, a reliable M^2-fit was not possible. However, we verified that the quite high M^2-value for the free dimension was mostly due to the laser ($M^2 = 2.1$ without waveguide) and not induced by the waveguide. As the pressure is increased from vacuum to 1.6 atm of Ar, the focal spot size in the free dimension increases by a factor of 1.85. Simultaneously, the focus position shifts about 2 cm towards the laser.

To sum up the above discussion, the nonlinear effects inside the waveguide, essential for pulse compression, simultaneously induce a finite astigmatism and reduce the focusability in the free waveguide dimension. However, both limitations can, in principle, be addressed by means of adaptive optics. Note, however, that the focusability constraints due to spectral and temporal inhomogeneity cannot be corrected by adaptive optics (see section 3.3). The astigmatism itself can be corrected, even without adaptive optics, simply by moving the collimating cylindrical mirror (see figure 1) towards the waveguide until the focal positions of both dimensions coincide. Thus the focal spot size at a pressure of 1.6 atm is less than a factor of two larger as compared to vacuum. Furthermore, as mentioned above, higher pulse energy laser systems deliver transverse beam profiles closer to top-hat, significantly reducing the problems of spatial phase and transverse inhomogeneity.

2.6. Optimization of input pulse duration

In order to optimize the input pulses for the compression, a programmable spectral amplitude and phase filter (DAZZLER, Fastlite) was installed in the laser chain before the regenerative amplifier. With this device, the spectral phase of the laser output pulses could be significantly flattened and the duration of the driving pulses for the planar hollow waveguide compression was reduced to 37 fs (FWHM). Additionally, a slightly shorter focal length ($f = 110$ cm, CVI) cylindrical mirror was used to focus the beam onto the waveguide entrance, improving the coupling to the fundamental waveguide mode. While the input laser pulse energy decreased slightly due to the implementation of the spectral filter, the waveguide throughput increased to about 80% and 10.6 mJ pulse energy was obtained at the output of the cell. Simultaneously, due to the shorter input pulse duration and the precise control of the input chirp, the pulse duration after compression was reduced to 10.13 ± 0.33 fs at 1.5 atm of Ar in the gas cell. Figure 8(a)

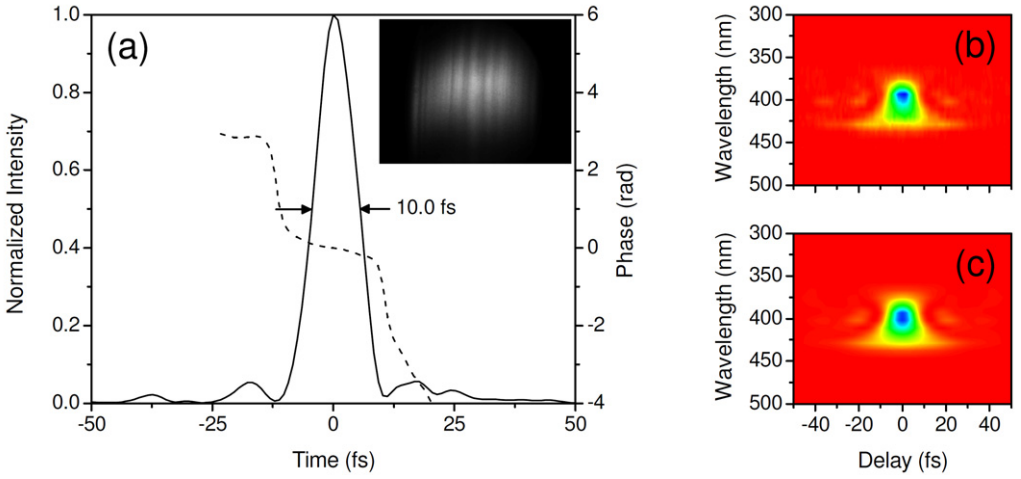

Figure 8. Temporal profile after compression at 1.5 atm of Ar and 37 fs input duration (a); the inset shows the output mode profile. Measured (b) and retrieved (c) SHG FROG traces.

shows a typical measured temporal intensity profile and phase as well as the output mode. The temporal profile is very clean, with two prepulses of less than 5% of the peak power. In figures 8(b) and (c), the measured and retrieved SHG FROG traces are plotted, respectively. The FROG error is 0.72% (128 × 128 matrix). Note that the shorter pulse duration after compression obtained here is mostly due to the optimization of the input pulse. The total level of nonlinearity, which determines the output mode quality and the focusability, remains unchanged.

Having evaluated in detail the characteristics (energy, duration, homogeneity and focusability) of the compressed output pulses of our experimental adaptation of the planar hollow waveguide compression scheme, we can perform a careful estimation of the vacuum intensity that the pulses can be focused to. If we consider a realistic reflective focusing system of numerical aperture NA = 0.36 (half focusing angle of 21°), and include conservative estimates for the focusability and the mean pulse duration, the focal intensity exceeds 10^{19} W cm^{-2} at few-cycle duration. This intensity level is well inside the regime of relativistic optics. This careful estimation emphasizes that the planar hollow waveguide compression scheme, as presented here, is capable of providing relativistic intensity at few-cycle duration, even with relatively simple table-top femtosecond lasers.

3. Theory and simulations

3.1. Basic waveguide theory

In this section, we shortly recall the basic theory of linear waveguide propagation. A planar hollow waveguide, guiding laser radiation in a gas-filled gap between two pieces of glass, is intrinsically leaky. The attenuation depends on the order of the guided modes, the separation of the glass plates and the laser polarization. The guided modes satisfy the Helmholtz equation and boundary conditions on the glass plates. They can be approximated as sine $V_{p=2m}(x) = \sin(p\pi x/2a)$ and cosine $V_{p=2m-1}(x) = \cos(p\pi x/2a)$ leaky waveguide modes with vanishing field at the glass surface [28], where p and m are integer numbers. Here, x is the transverse

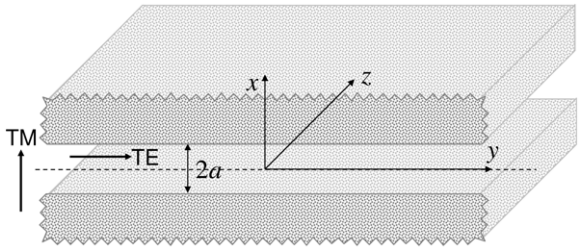

Figure 9. Coordinate system for the planar hollow waveguide. The arrows denote the polarization directions for TE and TM guided modes.

coordinate in the guided direction, y is the transverse coordinate in the free dimension, z is the propagation direction along the waveguide and $2a$ is the separation of the waveguide. See figure 9 for a sketch of the coordinate system with respect to the waveguide.

The waveguide modes form an orthogonal basis with

$$\frac{1}{a}\int_{-a}^{a} V_p(x)V_{p'}(x)\mathrm{d}x = \delta_{pp'}. \tag{1}$$

The modes can be distinguished in even and odd order depending on the mode index p. The lowest order odd mode with index $p = 1$ is also termed the fundamental waveguide mode. See figure 10(a) for a plot of the lowest order modes. The real part β_p and imaginary part α_p of the mode-dependent wave number $k_p = \beta_p + \mathrm{i}\alpha_p$ can be derived from perturbative analysis [29, 30]:

$$\beta_p(\omega)_{\mathrm{TE,TM}} = k(\omega)\sqrt{1 - \left(\frac{p\pi}{2k(\omega)a}\right)^2}, \tag{2}$$

$$\alpha_p(\omega)_{\mathrm{TE}} = \left(\frac{p\pi}{2k(\omega)a}\right)^2 \frac{1}{a\sqrt{n_{\mathrm{g}}^2 - 1}}, \quad \alpha_p(\omega)_{\mathrm{TM}} = \left(\frac{p\pi}{2k(\omega)a}\right)^2 \frac{n_{\mathrm{g}}^2}{a\sqrt{n_{\mathrm{g}}^2 - 1}}. \tag{3}$$

Here, $k(\omega)$ is the frequency-dependent free space wave number for a particular gas inside the waveguide. Equations (2) and (3) define the mode-dependent dispersion $\beta_p(\omega)$ and absorption $\alpha_p(\omega)$ relations, respectively. Note that, depending on the gas pressure and the waveguide separation, the group velocity and the group velocity dispersion can be significantly different from the free space dispersion relation. The real part of the wave number does not depend on the laser input polarization. It is the same for both TE and TM modes (see figure 9). The attenuation, however, is by a factor of n_{g}^2 greater for TM modes, where n_{g} is the refractive index of the glass material [28]. The attenuation is proportional to the square of the mode index p. Higher-order modes are therefore damped much more strongly than the fundamental mode ($p = 1$). See figure 10(b) for the relative attenuation of modes of different order along the waveguide.

We will now analyze the coupling of a laser beam focused with a cylindrical mirror to the entrance of the planar hollow waveguide. The incoming laser field $E(x, y)$ is decomposed into waveguide modes with amplitudes $A_p(y)$ as it enters the waveguide:

$$A_p(y) = \frac{1}{a}\int_{-a}^{a} V_p(x)E(x, y)\,\mathrm{d}x. \tag{4}$$

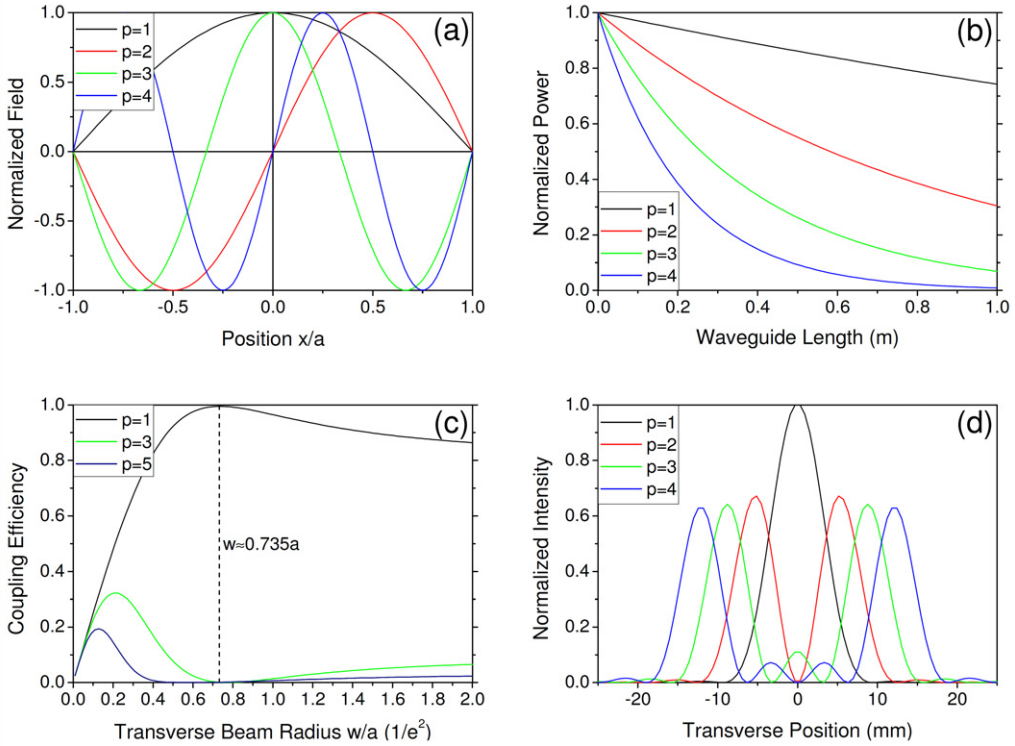

Figure 10. (a) Even and odd waveguide modes. (b) Attenuation for different modes. (c) Coupling efficiency for odd-order modes. (d) Far-field intensity patterns of guided modes (1 m distance).

For the sake of simplicity, we assume that the focal beam profile is Gaussian in x (guided dimension) and uniform in y (free dimension) $E(x, y) = E_0 \exp(-(x - x_0)^2/w^2$, with flat spatial phase. If the focused beam is centered exactly in the middle of the waveguide gap ($x_0 = 0$), only symmetric (odd-order) modes are excited. The coupling efficiency depends on the Gaussian width w of the beam compared to the half-width a of the waveguide. In figure 10(c), we plot the coupling efficiency to the first three odd-order modes as a function of Gaussian width. Optimized coupling conditions are found for $w \approx 0.735a$. In this case, about 99.4% of the power falling inside the waveguide ($-a \leqslant x \leqslant a$) and 98.8% of the total power are coupled to the fundamental waveguide mode ($p = 1$). Additionally, the first higher-order odd mode ($p = 3$) is damped nine times more strongly than the fundamental mode. Thus higher-order mode content is efficiently cleaned in the waveguide. Nonetheless, if the focus is shifted from the center of the waveguide or exhibits asymmetry, even order modes are also excited, whereas the lowest order even mode ($p = 2$) is damped only four times more strongly than the fundamental. Finally, figure 10(d) shows the far-field (1 m distance) intensity profiles of the lowest order modes for a waveguide separation of $2a = 127\ \mu$m.

3.2. Nonlinear pulse propagation in planar hollow waveguides

In the preceding section the linear properties of planar hollow waveguides were discussed. However, as in the experiments, the waveguide is applied to nonlinearly broaden the spectrum

of injected high-energy ultrashort laser pulses, in order to subsequently compress the pulses to shorter duration, the propagation inside the waveguide is intrinsically nonlinear. In the linear regime, individual modes, once excited at the entrance of the waveguide, propagate independently from each other. In contrast, in the nonlinear regime, waveguide modes exchange energy due to nonlinear coupling effects, such as Kerr self-focusing and plasma defocusing due to ionization.

In order to numerically describe nonlinear ultrashort pulse propagation inside a gas-filled planar hollow waveguide, a unidirectional nonlinear envelope equation (NEE) (5) is applied [31]–[33]. This type of equation is known to be valid for pulses down to the single-cycle regime [31]. Equation (5) was derived from the nonlinear Helmholtz equation and the method proposed by Feit and Fleck was used to introduce unidirectional propagation [34].

$$\partial_z \tilde{E}(k_\mathrm{T}, z, \omega) = \mathrm{i}\Delta k_z(k_\mathrm{T}, \omega)\tilde{E}(k_\mathrm{T}, z, \omega) + \frac{1}{k_z(k_\mathrm{T}, \omega)}\mathcal{F}\{N(x, y, z, t)\}\,. \tag{5}$$

Here, $\tilde{E}(k_\mathrm{T}, z, \omega)$ is the three-dimensional Fourier transform of the electric field envelope $E(x, y, z, t)$, $k_\mathrm{T} = \sqrt{k_x^2 + k_y^2}$ is the transverse wave number and $k_z(k_\mathrm{T}, \omega) = \sqrt{k^2(\omega) - k_\mathrm{T}^2}$ is the wave number in the propagation direction. The linear part of (5) describes the effects of diffraction, non-paraxiality and group velocity dispersion via a longitudinal wave number shift $\Delta k_z(k_\mathrm{T}, \omega) \equiv k_z(k_\mathrm{T}, \omega) - k_0 - (\omega - \omega_0)/v_\mathrm{g}$, originating firstly from the fact that the carrier wave $\exp(\mathrm{i}k_0 z)$ is canceled out in the transformation of the unidirectional propagation equation for the electric field into an NEE, and secondly from the description of the propagation in the local reference frame moving at group velocity $v_\mathrm{g} = (\mathrm{d}k(\omega)/\mathrm{d}\omega|_{\omega=\omega_0})^{-1}$ of the propagated pulse, where ω_0 is the center frequency. In the paraxial regime ($k_\mathrm{T} \ll k(\omega)$), which is a well-satisfied approximation in the context of our work, the explicit consideration of the k_T dependence of k_z is not essential in the nonlinear terms [33]. The following approximations were thus made: $k_z \approx k(\omega) - [k_\mathrm{T}^2/2k(\omega)]$ for the linear part and $k_z \approx k(\omega)$ in front of the nonlinear part. The dispersion relation $k(\omega) = (\omega/c)n(\omega)$ is calculated from the refractive index data of particular gases [35]. Therefore, no expansion of the dispersion around the center frequency is required. Nonlinear contributions to pulse propagation in (5) are gathered in $N(x, y, z, t)$, where $\mathcal{F}$ denotes a three-dimensional (3D) Fourier transform. We perform the following approximation $(1/k_z)\mathcal{F}\{N(x, y, z, t)\} \approx [1/k(\omega)]\mathcal{F}\{N(x, y, z, t)\} = \mathcal{F}\{N'(x, y, z, t)\}$ and write

$$N'(x, y, z, t) = \frac{\mathrm{i}}{2}\epsilon_0 n_0 n_2 \omega_0 T\,|E(x, y, z, t)|^2\,E(x, y, z, t) - \frac{\mathrm{i}}{2}\sigma\tau_\mathrm{c}\omega_0 T^{-1}\rho E(x, y, z, t) - \frac{1}{2}\left(\sigma\rho + U_\mathrm{i}\frac{W_\mathrm{PI}(I)}{I}(\rho_\mathrm{at} - \rho)\right)E(x, y, z, t). \tag{6}$$

The first term in (6) describes self-focusing and SPM due to the optical Kerr effect. We neglect the retarded Kerr response, since only noble gases will be considered. Here, c is the vacuum speed of light, ϵ_0 is the dielectric permittivity and $n_2 = 0.98 \times 10^{-19}\,\mathrm{cm^2\,W^{-1}}$ is the nonlinear refractive index for Ar at atmospheric pressure [36]. The second term in (6) stands for refraction due to generated free electrons of density $\rho(x, y, z, t)$. Here, $\sigma = e^2/m_\mathrm{e}c\epsilon_0 n_0 \tau_\mathrm{c}\omega_0^2$ is the cross section for inverse bremsstrahlung in the well-verified limit of a collision frequency much smaller than the laser frequency [37], and m_e is the free electron mass. The collision time $\tau_\mathrm{c} = 190\,\mathrm{fs}$ denotes the mean free time between collisions of free electrons with heavy particles (atoms) in Ar at atmospheric pressure [10]. The last term in (6) accounts for absorption due to inverse bremsstrahlung and nonlinear photoionization. Here, U_i denotes the ionization potential

and $\rho_{\mathrm{at}} = 2.5 \times 10^{25}\,\mathrm{m}^{-3}$ is the atomic density at atmospheric pressure and room temperature. The rate of nonlinear photoionization $W_{\mathrm{PI}}(I)$ is calculated from the generalized Keldysh PPT (Perelomov–Popov–Terent'ev) theory [38, 39], where $I(x, y, z, t)$ is the electric field intensity. The T-operator in (6) accounts for self-steepening effects. It is most conveniently applied in its frequency space representation $\tilde{T} = \omega/\omega_0$.

In order to calculate the density of generated free electrons $\rho(x, y, z, t)$, the following rate equation is solved in parallel with (5):

$$\frac{\partial \rho(x, y, z, t)}{\partial t} = W_{\mathrm{PI}}(I)\,(\rho_{\mathrm{at}} - \rho) + \frac{\sigma}{U_{\mathrm{i}}} I \rho. \tag{7}$$

Equation (5) describes nonlinear optical pulse propagation in free space. To adapt it to nonlinear propagation inside a planar hollow waveguide, we make use of the two different but equivalent representations of the laser pulse inside the waveguide, either as the electric field envelope itself or as the sum of the guided modes $A_p(y, z, t)$.

$$E(x, y, z, t) = \sum_{p=1}^{\infty} V_p(x) A_p(y, z, t), \tag{8}$$

where, for convenience, we chose the carrier of the fundamental mode $\exp(\mathrm{i}\beta_0 z)$ with $\beta_0 = \beta_{p=1}(\omega)|_{\omega=\omega_0}$ as the reference carrier wave to define the mode envelopes. The electric field envelope defined in (8) thus differs from that of (5) by a factor $\exp(\mathrm{i}(\beta_0 - k_0)z)$, and each mode envelope implicitly includes a longitudinal phase shift $\beta_p - \beta_0$ responsible for mode beatings. We can move from one representation to the other either by projecting the electric field to the modes via (4) or by reconstructing the field from the modes using (8). If we insert the 2D Fourier transform $\tilde{A}_p(k_y, z, \omega)$ of the guided mode representation with wave number $\beta_p(\omega)$ and absorption $\alpha_p(\omega)$ in (5), the following propagation equation is obtained:

$$\partial_z \sum_{p=1}^{P} \tilde{A}_p(k_y, z, \omega) V_p(x) = \mathrm{i} \sum_{p=1}^{P} \left(\Delta\beta_p(k_y, \omega) + \mathrm{i}\alpha_p(\omega)\right) A_p(k_y, z, \omega) V_p(x) + \mathcal{F}\left\{N'(x, y, z, t)\right\}. \tag{9}$$

In this context, $\mathcal{F}$ denotes just a 2D Fourier transform, since decomposition in transverse wave numbers for the guided dimension (x) is not necessary and $\Delta\beta_p(k_y, \omega) \equiv \sqrt{\beta_p^2(\omega) - k_y^2} - \beta_0 - (\omega - \omega_0)/v_{\mathrm{g},0}$. The frequency dependence of the wave number $\beta_p(\omega)$ and absorption coefficient $\alpha_p(\omega)$ is fully known and can be directly applied for each mode without approximation. The reference frame now moves at the group velocity $v_{\mathrm{g},0} = (\mathrm{d}\beta_{p=1}(\omega)/\mathrm{d}\omega|_{\omega=\omega_0})^{-1}$ of the fundamental mode, as it propagates the fastest. Higher order modes fall behind along propagation inside the waveguide.

We numerically solve (9) in a split-step scheme, where the linear and nonlinear parts are propagated alternately. The linear step can be exactly performed by propagating the 2D Fourier transform of each mode $\tilde{A}_p(k_y, z, \omega)$ in mode space as $\tilde{A}_p(k_y, z + \Delta z, \omega) = \tilde{A}_p(k_y, z, \omega) \exp\left(\mathrm{i}\left(\Delta\beta_p(k_y, \omega) + \mathrm{i}\alpha_p(\omega)\right)\Delta z\right)$. The nonlinear step is evaluated in normal space except for T-operators, which are applied in frequency space. $N'(x, y, z, t)$ was not rederived using $\beta_{p=1}(\omega)$ instead of $k(\omega)$. This is within the range of approximations made before, preserving the lowest order frequency dependence. Between a linear and a nonlinear step, the electric field $E(x, y, z, t)$ is reconstructed from the modes, then a nonlinear step is performed and subsequently the field is projected back on the modes to perform the next linear step.

Note that this approach of continuously going back and forth between normal space and mode space representation is strictly different from traditional coupled mode theory [36, 40], where the propagation equation is integrated in mode space only. In coupled mode theory, usually only the coupling between the fundamental and higher-order modes is considered, but not the coupling between individual higher-order modes. In contrast, our scheme intrinsically includes the coupling between all modes involved. Additionally, it is more convenient to numerically implement than coupled mode theory. In order to properly describe beatings between different guided coupled modes with different wave numbers and group velocities, the maximum possible step size is limited to $\Delta z \ll 2\pi/(\beta_1 - \beta_P)$. Here, P is the index of the highest mode excited with significant amplitude and $2\pi/(\beta_1 - \beta_P)$ is the beating length between the fundamental mode and the mode of order P.

3.3. Simulations

In section 2, an almost fourfold compression of energetic ultrashort laser pulses to 10.1 fs at 80% energy throughput, focusable to relativistic intensity, was presented, based on the planar hollow waveguide compression scheme. The energy level is superior compared to the use of filamentation or hollow capillaries for compression. Two main aspects of the planar hollow waveguide compression scheme were identified, which have to be carefully considered in applications: firstly, the deterioration of the transverse output mode in the free waveguide dimension, limiting the shortest possible pulse duration, and secondly, a reduced focusability due to non-uniform spectrum and duration as well as a retarded spatial phase also in the free dimension. Both aspects can be addressed using the waveguide propagation model based on equation (9) presented in the previous section.

Numerical simulations of pulse compression in planar hollow waveguides were published in an earlier paper (Arnold *et al* [22]), showing convincing general agreement between experimental compression results and simulations based on (9). This was illustrated in terms of comparing three different quantities for measured and simulated compressed pulses (see figure 2 in [22]): the temporal compressed pulse profiles, the spectrograms for SHG FROG, as well as the output modes. The experimental results used in this comparison can be found in Akturk *et al* [21], where we reported a compressed pulse duration of 13.6 fs at an output pulse energy of 8.1 mJ. These results were obtained with the same experimental setup as illustrated in figure 1, with a waveguide made from fused silica (see section 2.2), at 1.5 atm of Ar and 127 μm separation. In [22] we used these parameters to carefully adapt the numerical model to the experimental results. In order to obtain good agreement between simulations and experiments, the initial conditions for the model were chosen to match the experimental conditions as closely as possible. In particular, instead of using a perfect Gaussian initial pulse, a measured temporal profile (Grenouille, Swamp Optics) was implemented. Furthermore, the transverse structure of the output mode, observed along the free waveguide dimension (see e.g. figure 5(a)), was well reproduced numerically, when a measured transverse beam profile was used as an initial condition. The difference between applying an ideal transverse beam profile and applying a measured profile is illustrated in figure 11, where we compare the fluence in the free waveguide dimension for a perfect Gaussian initial profile (a) and the actual measured beam profile (b). For the sake of simplicity, we choose the same parameters as in [22] for the simulations throughout this paper, although the output pulse energy was increased and the compressed duration decreased simultaneously (see section 2), as compared to [21, 22]. It is evident that

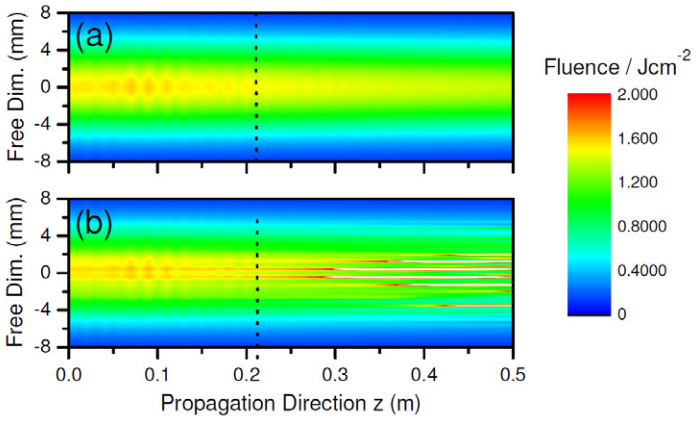

Figure 11. Fluence along the free waveguide dimension with an ideal Gaussian transverse input beam profile (a) and a measured beam profile (b).

the distinct transverse structure in figure 11(b) emerges from small-scale self-focusing of initial beam imperfections and noise. The dotted line in both plots indicates the length of the waveguide (21 cm) used in the experiments. For the case in figure 11(b), the waveguide length is obviously close to the maximum permissible propagation distance at this level of nonlinearity. Shortly afterwards, the beam finally breaks up into individual filaments, not usable for applications. For figure 11(a), however, the distance of stable transverse propagation is greatly overestimated. The beam indeed breaks up into transverse filaments after about 80 cm due to modulational instability emerging from numerical noise. Any real laser beam would, of course, break up before.

Having identified that the transverse instability due to small-scale self-focusing limits the maximum propagation distance in the waveguide at a given level of nonlinearity, a numerical stability analysis was performed in order to investigate possible scalability to higher pulse energy [22]. Since the scalability to high pulse energy is the striking advantage of the hollow planar waveguide compression scheme compared to hollow capillaries and filamentation, we will recall this aspect here. In order to identify a regime of stable transverse propagation inside the waveguide, which can be utilized for pulse compression, we evaluate the length scales for instabilities to be avoided, such as self-focusing of the entire beam and disintegration of the transverse profile due to small-scale self-focusing and modulational instability, respectively. The regime of stable propagation is illustrated in figure 12. Propagation in the waveguide is stable when the length for self-focusing of the entire beam (blue dotted line) is much longer than the length of the waveguide, and when the length for transverse disintegration of the mode due to modulational instability is also longer than the waveguide. A derivation of an analytic formula for the 1D self-focusing length is given in [22]. Along the y-direction in figure 12, the distance after which instabilities were numerically observed is plotted, either for a perfect input transverse beam profile (black triangles) or for the measured beam profile of our laser (red circles). The length of the experimental waveguide is indicated by a dotted line. To scale to higher pulse energy, we gradually increase the beam size w_y in the free waveguide dimension (bottom x-axis) at constant intensity. The pulse energy (top x-axis) and total power in the waveguide scale linearly with the beam size. The measured transverse beam input profile is simply scaled with the transverse beam size w_y. The other numerical parameters, such as intensity, pulse duration, waveguide separation, choice of gas

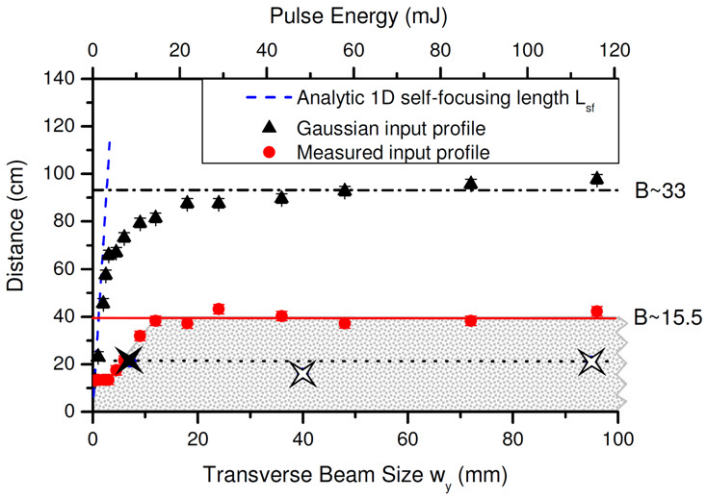

Figure 12. Maximum distance of stable waveguide propagation versus transverse beam size (free dimension) and pulse energy, respectively. The shaded area indicates the stability region for the measured input profile of our laser.

(Ar) and pressure, remain unchanged, since it was experimentally confirmed that this set of parameters corresponds to a good compression regime with well-behaved mode dynamics [22]. It is evident from figure 12 that the maximum distance of stable propagation is much shorter when a measured transverse beam profile is considered instead of a perfect beam. Indeed, the quality of the input beam to the waveguide determines the maximum distance of stable propagation. The shaded area indicates the regime of stable propagation, determined by our experimental beam profile. For small transverse beam size w_y, the stability region is limited by self-focusing of either the whole beam or individual structures in the beam profile. For larger beam size the maximum propagation distance is limited by modulational instability emerging from small inhomogeneities and noise in the beam profile [41]. The solid star in the stability region indicates the position of the experimental compression published in [21] and numerically simulated in [22]. This combination of parameters is located very close to the boundary of the stable region. For slightly longer propagation distance the beam breaks up into individual filaments (see figure 11), unusable for compression. The stability analysis presented in figure 12 has been performed for a constant level of nonlinearity, keeping the nonlinear refractive index n_2 (fixed by the choice of the gas), the gas pressure p_g (in atm) and the intensity I_0 constant. However, the stability region is generally valid for $I_0 n_2 p_g = \text{const}$, as long as the intensity level remains below excessive ionization. Thus different noble gases, input intensities and pressures can also be applied without compromising stable propagation. In our simulations, the input intensity $I_0 = 3.35 \times 10^{13}\,\mathrm{W\,cm^{-2}}$ keeps the density of generated free electrons well below $10^{15}\,\mathrm{cm^{-3}}$ for 1.5 atm of Ar. In order to limit the impact of ionization, the input intensity must be decreased for noble gases with lower ionization potential (Kr and Xe), whereas it could be increased for Ne and He. Note that, if the pulse duration is varied, only the bottom x-axis (beam size w_y) in figure 12 remains valid.

For large transverse beam size ($w_y \gtrsim 20\,\mathrm{mm}$), the stability regime is determined by modulational instability. In this case the maximum propagation distance z can be associated with a specific value of the B-integral $B \approx k_0 I_0 n_2 p_g z$, offering additional freedom to also vary

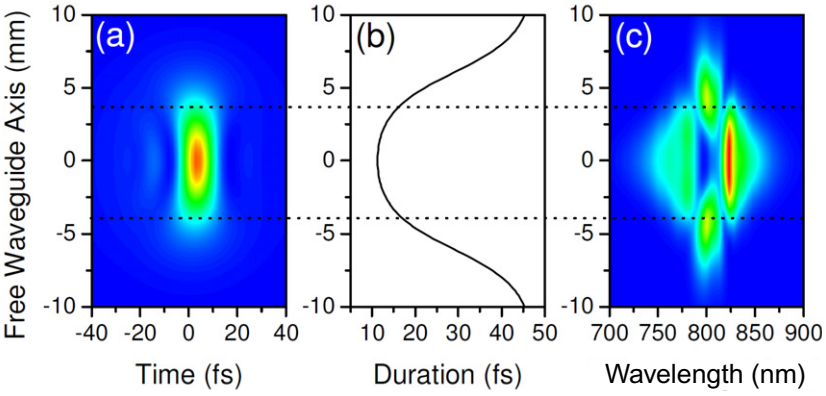

Figure 13. Temporal intensity (a), transverse pulse duration (FWHM) (b) and spectral intensity (c) versus the free waveguide dimension.

the length of the planar hollow waveguide. While for the experimental conditions (solid star) a value of $B \approx 8$ could not be exceeded, for larger beam size a B-value of about 15.5 defines the boundary of the stable region, potentially allowing for larger compression ratios.

Applying the above considerations, we indicated two additional points in the stability diagram (open stars). One corresponds to the compression of pulses at the 100 mJ energy level to few-cycle duration below 10 fs, and the other corresponds to the compression of pulses, which are already at few-cycle duration. Specific parameters and a detailed description of the two cases can be found in [22]. The first scenario particularly emphasizes the suitability of the planar hollow waveguide concept to energy regimes unlikely to be accessible with filamentation or hollow capillaries. Additionally, the compressible energy could be further enhanced by using noble gases with higher ionization potentials (Ne and He). With a proper choice of the gas pressure to adjust the nonlinearity, the energy level compared to the 100 mJ case suggested in [22] could be increased by roughly a factor of ≈ 3 for Ne and ≈ 5 for He. The low nonlinearity, in particular for He, would, however, require a specific design of the gas cell, able to withstand pressures much above atmospheric [42]. The extrapolated peak intensity of $\approx 2 \times 10^{14}\,\mathrm{W\,cm^{-2}}$ for He should not be critical for the waveguide, provided that coupling conditions are good. It has been shown that peak intensities higher than $10^{15}\,\mathrm{W\,cm^{-2}}$ can be propagated inside hollow capillaries without wall damage [43, 44]. Furthermore, the waveguide separation could be increased to lower the intensity in the waveguide.

Following the experimental results, we now also address the transverse homogeneity and the focusability of the compressed output mode numerically. Figure 13 shows the spatio-temporal intensity profile of the compressed pulse (a), the transverse pulse duration (FWHM) (b) and the transverse spectrum (c) in the free waveguide dimension. For the sake of simplicity, a clean Gaussian transverse beam profile was considered here. It is evident that pulse duration and spectral broadening strongly depend on the transverse position. The two dotted lines indicate the interval of pulse duration shorter than 1.5 times the on-axis duration. As performed in section 2 for the experimental case, we can again calculate the percentage of total pulse energy contained in this interval. The value of about 71% is in striking agreement with the value of 67.6% obtained experimentally. Spectral splitting due to SPM is numerically more pronounced as compared to the experiments. It can, however, also be observed experimentally

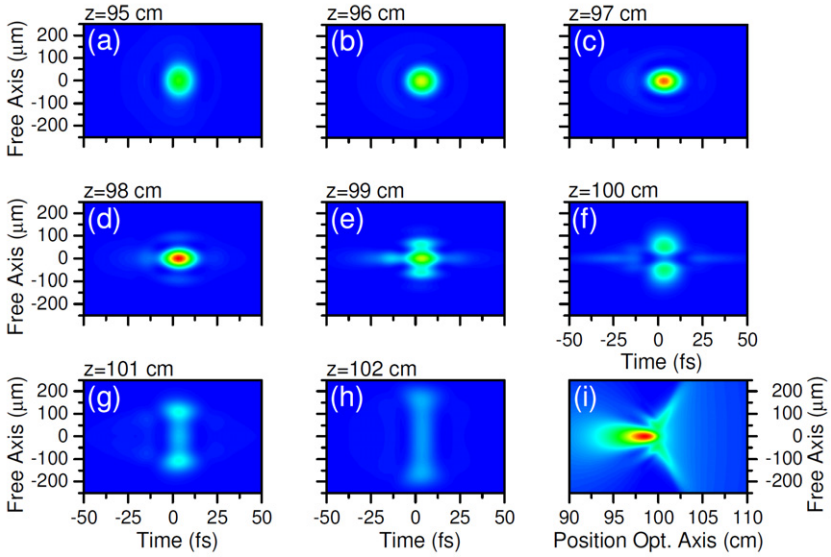

Figure 14. Focusing of the free waveguide dimension of the compressed output pulse with an $f = 1$ m focal length: (a–h) spatio-temporal intensity profiles at various positions on the optical axis in the vicinity of the geometrical focus; (i) fluence versus position.

in figure 5(b). Note that pulse duration, spectral broadening and spatial phase vary only along the free waveguide dimension; the guided dimension features homogeneous beam characteristics.

Having in mind that high-power ultrashort pulse lasers typically have a more square-like or top-hat transverse beam profile, different from the Gaussian profile considered here, we also calculated the transverse homogeneity for super-Gaussian beam profiles. For a super-Gaussian beam of order four, 85.6% of the total pulse energy falls within the interval of 1.5 times the on-axis duration; for a super-Gaussian profile of order ten, it is 93.5%. Consequently, a compressed pulse at the 100 mJ energy level as proposed in [22] would feature significantly more homogeneous transverse spectrum and duration as compared to figure 13.

Finally, we also numerically investigate the focusability of the compressed pulse. As the guided waveguide dimension features homogeneous spectrum, and duration, as well as flat spatial phase, it focuses intrinsically well. The discussion of focusability therefore concentrates on the free waveguide dimension. As discussed in section 2, there are three factors in the planar hollow waveguide compression scheme that potentially limit the focusability of the output pulse: (i) the transverse structure in the beam, (ii) the retarded phase along the output beam profile and (iii) the transversely inhomogeneous spectrum and duration. We will evaluate the impact of each factor and point out possible improvements. In order to study the focusability, we use frequency-dependent diffraction theory as required for broadband pulses [45]. First, the electric field on the collimating cylindrical mirror (see figure 1) is calculated. As the beam expands rapidly after the end of the waveguide, we neglect nonlinear propagation in the gas medium and the output thin window of the gas cell. We numerically study the refocusing of the free waveguide axis with a focusing mirror. For the sake of simplicity, we chose the same focal length ($f = 1$ m) as in the experiments. Figures 14(a)–(h) show on-axis spatio-temporal intensity profiles at different positions z along the optical axis in the vicinity of the focus (95–102 cm). The fluence along

the optical axis is plotted in (i). Several features can be extracted from figure 14. Firstly, the pulse focuses at $z \approx 98$ cm, 2 cm before the actual focal length ($f = 100$ cm), indicating an astigmatism. Secondly, the transverse size of the smallest focal spot (figure 14(d)) is larger as compared to optimum focusing. Both effects, the focal shift and the reduction in focusability, were also experimentally recognized, as discussed in section 2. The shift of the focal position towards the laser of about 2 cm experimentally (see figure 7) and numerically is in striking agreement. This is an additional valuable verification of the appropriateness and accuracy of the numerical modeling. Another interesting feature observable from figure 14 is that the long pulse durations located in the wings of the transverse profile, where almost no phase retardation occurs, focus close to the actual geometric focal position ($z = 100$ cm). The split intensity distribution at the focal position (figure 14(f)) is due to on-axis interference of the 'long' wings with the 'short' center of the beam. The focal shift can also be understood as a time gate, separating the short part from the long part of the beam. This can, however, also be achieved by cutting the 'long' wings of the profile with an appropriate aperture.

While the astigmatism resulting in the focal shift can clearly be associated with the phase retardation along the transverse beam profile, the reduction in focusability is due to the transverse structure, the retarded phase and the non-uniform duration and spectrum. To evaluate the impact of each effect, we compare focal intensities with the different effects numerically switched on and off. The impact of the transverse mode structure can easily be estimated by using an ideal Gaussian beam instead of the measured profile. The influence on the focusability is found to be small; the maximum focal intensity is reduced by less than 2% if the measured input beam profile is used. The influence of the retarded phase can be studied by artificially flattening the transverse spatial phase. Experimentally, this can be performed with an appropriate adaptive mirror. If we compare the focal intensity of the pulse with the corrected spatial phase with the uncorrected one, an increase in the peak intensity of about 33% is observed. The spatio-temporal focal intensities with correction of the spatial phase are plotted in figure 15(a)–(h) at the same positions along the optical axis as in figure 14. Correction of the spatial phase reduces the focal spot size, increases the focal intensity and removes the astigmatism simultaneously. Note that the fluence figure 15(i) is almost symmetric around the geometrical focus. The remaining discrepancy is due to higher-order spatial phase, which cannot easily be corrected.

We evaluated that the focal intensity can be increased by about 33% if the spatial phase is corrected by adaptive optics. However, the strongest impact on the focusability is due to the transverse temporal and spectral inhomogeneity. An ultrashort laser pulse with an inhomogeneous spatial duration, as shown in figure 13, intrinsically focuses to a larger spot as compared to a pulse with homogeneous spectrum and duration. If we compare the focal intensity to a pulse of the same energy, which was artificially homogenized to the on-axis spectrum and duration, a 56% higher focal intensity is observed. This accounts for a Strehl ratio of about 64% for the case of corrected spatial phase by means of adaptive optics, and about 48% for the uncorrected pulse. However, the reduced focusability appears only for the free waveguide axis, whereas the guided axis focuses almost perfectly. Again, we also investigated the focusability for more square-like, super-Gaussian transverse beam profiles. The transverse spectrum, duration and phase are more homogeneous along the free waveguide axis for super-Gaussian beams. Thus, the impact of these features on the focusability is less pronounced as compared to a Gaussian beam profile. For all super-Gaussian profiles (order 4–10) investigated, the focal intensity is reduced by less than 30% for an uncorrected pulse (without adaptive

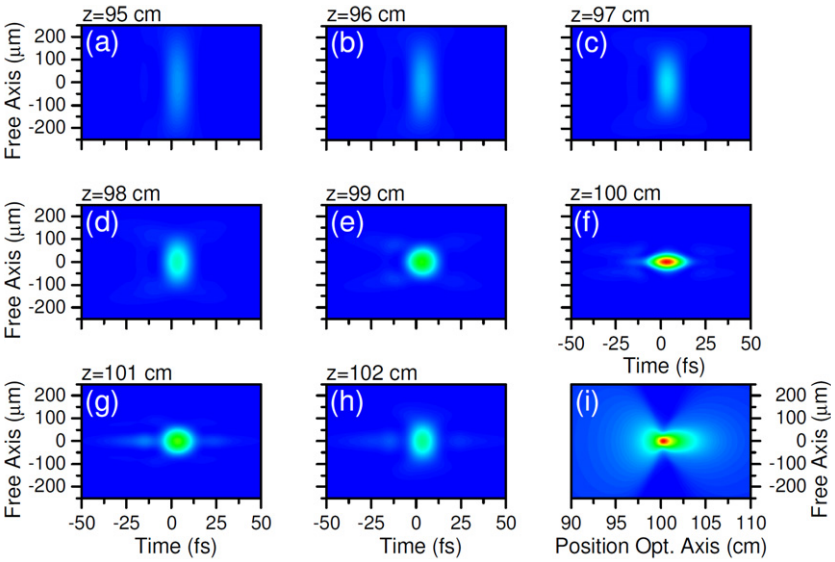

Figure 15. The same plot as figure 14, but for a pulse with corrected spatial phase.

optics), as compared to a pulse with flattened phase and artificially homogenized spectrum and duration. Hence, adaptive optics is not obligatory.

4. Conclusion

A comprehensive overview of the planar hollow waveguide scheme for the compression of ultrashort laser pulses to the few-cycle regime and its experimental adaptation was presented. The key benefit of the concept, as compared to the most common compression techniques using hollow capillaries and filamentation, is the superior scalability to high pulse energy. Simultaneously, the transverse nonlinear dynamics in the free waveguide dimension influences the output mode quality and the shortest possible pulse duration, respectively, as well as the focusability of the output pulse. These aspects were carefully addressed, both experimentally and numerically, and possible improvements were highlighted. We report the experimental results of 10.6 mJ output pulse energy at 80% energy throughput and shortest pulse duration of 10.1 fs (FWHM) after compression. The output pulses were characterized in detail in terms of transverse homogeneity, spatial phase and focusability. A careful estimation reveals that the compressed pulses should be focusable to relativistic intensity exceeding 10^{19} W cm^{-2} at few-cycle duration. The experimental results are in excellent agreement with numerical simulations based on a nonlinear waveguide propagation model. Based on this model, the region of stable waveguide propagation and its impact on energy scalability were investigated. We point out that the energy level of 100 mJ for the compression of ultrashort pulses to the few-cycle regime, as proposed in [22], could, in principle, be further increased by the choice of noble gases with higher ionization potential (Ne and He), as well as by increasing the waveguide separation. Furthermore, as the transverse beam profile for such powerful lasers is typically more square-like, output pulses would feature more homogeneous transverse beam characteristics with a significantly reduced impact on the focusability.

Acknowledgment

We gratefully acknowledge the funding of CLA's work by the Deutsche Akademie der Naturforscher Leopoldina (grant no. BMBF-LPD 9901/8-181).

References

[1] Krausz F and Ivanov M 2009 Attosecond physics *Rev. Mod. Phys.* **81** 163–234
[2] Esarey E, Schroeder C B and Leemans W P 2009 Physics of laser-driven plasma-based electron accelerators *Rev. Mod. Phys.* **81** 1229–85
[3] L'Huillier A *et al* 1995 High-order harmonics—a coherent source in the XUV range *J. Nonlinear Opt. Phys. Mater.* **4** 647–65
[4] Goulielmakis E 2008 Single-cycle nonlinear optics *Science* **320** 1614–7
[5] Nisoli M, De Silvestri S, Svelto O, Szipöcs R, Ferencz K, Spielmann Ch, Sartania S and Krausz F 1997 Compression of high-energy laser pulses below 5 fs *Opt. Lett.* **22** 522–4
[6] Hauri C P, Kornelis W, Helbing F W, Heinrich A, Couairon A, Mysyrowicz A, Biegert J and Keller U 2004 Generation of intense, carrier-envelope phase-locked few-cycle laser pulses through filamentation *Appl. Phys.* B **79** 673–7
[7] Suda A, Hatayama M, Nagasaka K and Midorikawa K 2005 Generation of sub-10-fs, 5-mJ-optical pulses using a hollow fiber with a pressure gradient *Appl. Phys. Lett.* **86** 111116
[8] Bohman S, Suda A, Kaku M, Nurhuda M, Kanai T, Yamaguchi S and Midorikawa K 2008 Generation of 5 fs, 0.5 TW pulses focusable to relativistic intensities at 1 kHz *Opt. Express* **16** 10684–9
[9] Fourcade Dutin C, Dubrouil A, Petit S, Mével E, Constant E and Descamps D 2010 Post-compression of high-energy femtosecond pulses using gas ionization *Opt. Lett.* **35** 253–5
[10] Couairon A, Biegert J, Hauri C P, Kornelis W, Helbing F W, Keller U and Mysyrowicz A 2006 Self-compression of ultrashort laser pulses down to one optical cycle by filamentation *J. Mod. Opt.* **53** 75–85
[11] Kosareva O G, Panov N A, Uryupina D S, Kurilova M V, Mazhorova A V, Savelev A B, Volkov R V, Kandidov V P and Chin S L 2008 Optimization of a femtosecond pulse self-compression region along a filament in air *Appl. Phys.* B **91** 35–43
[12] Roberts A, Shivaram N, Xu L and Sandhu A 2009 Optimization of few-cycle pulse generation: spatial size, mode quality and focal volume effects in filamentation based pulse compression *Opt. Express* **17** 23894–902
[13] Zair A, Guandalini A, Schapper F, Holler M, Biegert J, Gallmann L, Keller U, Couairon A, Franco M and Mysyrowicz A 2007 Spatio-temporal characterization of few-cycle pulses obtained by filamentation *Opt. Express* **15** 5394–404
[14] Mysyrowicz A, Couairon A and Keller U 2008 Self-compression of optical laser pulses by filamentation *New J. Phys.* **10** 025023
[15] Ishii N, Turi L, Yakovlev V S, Fuji T, Krausz F, Baltuska A, Butkus R, Veitas G, Smilgevicius V, Danielius R and Piskarskas A 2005 Multimillijoule chirped parametric amplification of few-cycle pulses *Opt. Lett.* **30** 567–9
[16] Dubietis A, Butkus R and Piskarskas A P 2006 Trends in chirped pulse optical parametric amplification *IEEE J. Sel. Top. Quantum Electron.* **12** 163–72
[17] Tavella F, Marcinkevicius A and Krausz F 2006 90 mJ parametric chirped pulse amplification of 10 fs pulses *Opt. Express* **14** 12822–7
[18] Herrmann D, Veisz L, Tautz R, Tavella F, Schmid K, Pervak V and Krausz F 2009 Generation of sub-three-cycle, 16 TW light pulses by using noncollinear optical parametric chirped-pulse amplification *Opt. Lett.* **34** 2459–61
[19] Nurhuda M, Suda A, Bohman S, Yamaguchi S and Midorikawa K 2006 Optical pulse compression of ultrashort laser pulses in an argon-filled planar waveguide *Phys. Rev. Lett.* **97** 153902

[20] Chen J, Suda A, Takahashi E J, Nurhuda M and Midorikawa K 2008 Compression of intense ultrashort laser pulses in a gas-filled planar waveguide *Opt. Lett.* **33** 2992–4
[21] Akturk S, Arnold C L, Zhou B and Mysyrowicz A 2009 High-energy ultrashort laser pulse compression in hollow planar waveguides *Opt. Lett.* **34** 1462–4
[22] Arnold C L, Akturk S, Franco M, Couairon A and Mysyrowicz A 2009 Compression of ultrashort laser pulses in planar hollow waveguides: a stability analysis *Opt. Express* **17** 11122–9
[23] Akturk S, D'Amico C and Mysyrowicz A 2008 Measuring ultrashort pulses in the single-cycle regime using frequency-resolved optical gating *J. Opt. Soc. Am.* B **26** A63–9
[24] Nibbering E T J, Grillon G, Franco M A, Prade B S and Mysyrowicz A 1997 Determination of the inertial contribution to the nonlinear refractive index of air, N_2 and O_2 by use of unfocused high-intensity femtosecond laser pulses *J. Opt. Soc. Am.* B **14** 650–60
[25] Dickinson J T, Orlando S, Avanesyan S M and Langford S C 2004 Color center formation in soda lime glass and NaCl single crystals with femtosecond laser pulses *Appl. Phys.* B **79** 859–64
[26] Shelton D P 1990 Nonlinear-optical susceptibilities of gases measured at 1064 and 1319 nm *Phys. Rev.* A **42** 2578–92
[27] Siegman A E 1986 *Lasers* (Sausalito, CA: University Science Books)
[28] Laakmann K D and Steier W H 1976 Waveguides: characteristic modes of hollow rectangular dielectric waveguides *Appl. Opt.* **15** 1334–40
[29] Marcatili E A J and Schmelzer R A 1964 Hollow metallic and dielectric waveguides for long distance optical transmissions and lasers *Bell Syst. Tech. J.* **43** 1783–809
[30] Yariv A 1989 *Quantum Electronics* 3rd edn (New York: Wiley)
[31] Brabec T and Krausz F 1997 Nonlinear optical pulse propagation in the single-cycle regime *Phys. Rev. Lett.* **78** 3282–5
[32] Couairon A and Mysyrowicz A 2007 Femtosecond filamentation in transparent media *Phys. Rep.* **441** 47–189
[33] Kolesik M and Moloney J V 2004 Nonlinear optical pulse propagation simulation: from Maxwell's to unidirectional equations *Phys. Rev.* E **70** 036604
[34] Feit M D and Fleck J A Jr 1988 Beam nonparaxiality, filament formation and beam breakup in the self-focusing of optical beams *J. Opt. Soc. Am.* B **5** 633
[35] Dalgarno A and Kingston A E 1966 The refractive indices and Verdet constants of the inert gases *Proc. R. Soc.* A **259** 424–9
[36] Tempea G and Brabec T 1998 Theory of self-focusing in a hollow waveguide *Opt. Lett.* **23** 762–4
[37] Yablonovitch E and Bloembergen N 1972 Avalanche ionization and the limiting diameter of filaments induced by light pulses in transparent media *Phys. Rev. Lett.* **29** 907–10
[38] Keldysh L V 1965 Ionization in the field of a strong electromagnetic wave *Sov. Phys.—JETP* **20** 1307–14
[39] Perelomov A M, Popov V S and Terent'ev M V 1966 Ionization of atoms in an alternating electric field *Sov. Phys.—JETP* **23** 924–34
[40] Courtois C, Couairon A, Cros B, Marques J R and Matthieussent G 2001 Propagation of intense ultrashort laser pulses in a plasma filled capillary tube: simulations and experiments *Phys. Plasmas* **8** 3445–56
[41] Bespalov V I and Talanov V I 1966 Filamentary structure of light beams in nonlinear liquids *Zh. Eksper. Teor. Fiz. Pis'ma Red.* **3** 471–6 (in Russian)
Bespalov V I and Talanov V I 1966 *JETP Lett.* **3** 307–10 (English translation)
[42] Goulielmakis E, Koehler S, Reiter B, Schultze M, Verhoef A J, Serebryannikov E E, Zheltikov A M and Krausz F 2008 Ultrabroadband, coherent light source based on self-channeling of few-cycle pulses in helium *Opt. Lett.* **33** 1407–9
[43] Dorchies F *et al* 1999 Monomode guiding of 10^{16} W/cm^2 laser pulses over 100 Rayleigh lengths in hollow capillary dielectric tubes *Phys. Rev. Lett.* **82** 4655–8
[44] Wagner N L, Gibson E A, Popmintchev T, Christov I P, Murnane M M and Kapteyn H C 2004 Self-compression of ultrashort pulses through ionization-induced spatiotemporal reshaping *Phys. Rev. Lett.* **93** 173902
[45] Gu M 2000 *Advanced Optical Imaging Theory* (Berlin: Springer)